

Asymmetric Electrostatic Dodecapole: Compact Bandpass Filter with Low Aberrations for Momentum Microscopy

O. Tkach, S. Babenkov, Y. Lytvynenko, O. Fedchenko, K. Medjanik, D. Vasilyev, H.-J. Elmers and G. Schönhense*

Johannes Gutenberg-Universität, Institut für Physik, 55128 Mainz, Germany

* corresponding author: schoenhe@uni-mainz.de

Abstract

Imaging energy filters in photoelectron microscopes and momentum microscopes employ spherical fields with deflection angles of 90° , 180° and even $2 \times 180^\circ$. These instruments are optimized for high energy resolution, yet they come along with image aberrations when they are operated in high transmission mode with medium energy resolution. Here we present a new approach for bandpass-filtered imaging in real or reciprocal space, using an asymmetric electrostatic dodecapole. This multipole enables energy-dispersive beam deflection and correction of image aberrations up to the 3rd order. Owing to a deflection angle of only 4° , the total beam displacement in the filter is just ~ 10 mm. Hence, the entire instrument is compact and just requires a straight vacuum tube. The multipole is framed by transfer lenses in the entrance and exit branch. Two sets of 16 entrance and exit apertures with different sizes on piezomotor-driven holders allow selecting the desired resolution. The combination of apertures and dodecapole acts as a bandpass pre-selector in a high-energy time-of-flight momentum microscope at the hard X-ray beamline P22 at PETRA-III (DESY, Hamburg). At pass energies between 400 and 600 eV it transmits electrons with kinetic energies in the range of 20-40 eV and thus effectively eliminates unwanted intensity from higher-energy electrons in the ToF analyzer. At low pass energies, the instrument allows energy-filtered imaging without subsequent ToF analysis. In a laboratory experiment the 4° prototype reached < 500 meV resolution, which is sufficient for fast survey studies in the X-ray range.

I. INTRODUCTION

Imaging bandpass filters play an important role in photoelectron spectroscopy. Such filters can either transport real-space images as studied in detail by Tonner [1] or momentum-space images as pioneered by Kirschner and coworkers [2]. The latter family of instruments established a new way of angle-resolved photoelectron spectroscopy (ARPES), termed momentum microscopy (MM). This early work initiated the development of various types of momentum microscopes [3-10], whose front lens converts the photoelectron angular distribution into a full-field image of the transversal momentum pattern (k_x, k_y). Dispersive-type MMs either employ a tandem arrangement of two hemispherical analyzers [2-6] or a single hemispherical analyzer [7-10]. Technically, these instruments resemble the spectroscopic low-energy electron microscope (SPELEEM) as developed by Bauer and coworkers [11,12].

In all these instruments energy-filtered 2D images (real or reciprocal space) are transported through the analyser by employing concepts of charged-particle optics and electron microscopy. Like in conventional spectrometers, the energy resolution is defined by pass energy and sizes of entrance and exit slits. A resolution of 4.2 meV has been reached using a single-hemisphere setup [8]. A different type of momentum microscope is based on time-of-flight (ToF) recording [13]. ToF-MMs simultaneously acquire an energy band of several eV width using a time-resolving image detector, facilitating 3D (E_{kin}, k_x, k_y) recording.

The hemisphere-based instruments involve one or two 180° deflections [1-10] or a 90° deflection [11,12] with corresponding transfer lens systems. Thus, these instruments come along with image aberrations when they are operated in high transmission mode with medium energy resolution. Here, we present a new design of a compact electrostatic bandpass filter, which fits into the linear column of a ToF-MM. We adopt the concept of an electrostatic dodecapole, as theoretically studied in detail by Boerboom et al. [14,15]. This type of multipole allows the superposition of dipole, quadrupole and hexapole fields and thus can correct image aberrations up to the 3rd order.

A prototype dodecapole is used as a pre-filter in a ToF-MM at the hard-X-ray beamline P22 at PETRA, where it significantly reduces the background signal and eliminates artefacts in the ToF spectra. At high kinetic energies, the so-called ‘temporal aliasing’ effect [16] can give rise to artefacts in spectra and momentum patterns. These artefact features originate from electrons, whose time of flight differ by multiples of the pulse period of the photon source in comparison with the flight time of the probe electrons of interest. The time-resolving detector cannot distinguish such (faster or slower) background electrons from the true signal. The energy-dispersive bandpass filter confines the recorded energy interval to the region of interest, thus completely eliminating the aliasing artefacts.

The dodecapole arrangement consists of an entrance and an exit branch, both hosting sets of 16 size-selectable and position-adjustable apertures, serving as entrance and exit apertures. The transmitted energy bandwidth depends on the pass energy and on the slit width as well as on the deflection angle. When used for pre-filtering, the dodecapole unit must not be operated with high energy resolution, because the desired final resolution is reached by the

ToF analysis. For the prototype, a small deflection angle of only 4° was chosen. This allows retaining a linear vacuum housing and a single mumetal tube for magnetic shielding.

At low pass energies and small entrance and exit apertures, this device can be operated as imaging filter with moderate energy resolution well below 1 eV even without ToF analysis. This mode enables taking survey spectra and fast core-level mapping like in conventional dispersive spectrometers.

II. The asymmetric dodecapole: A versatile device for energy filtering and aberration correction

II.A Motivation for the design of the dodecapole filter

The motivation for the development of an asymmetric dodecapole originated from an inherent problem of the ToF method when recording wide kinetic-energy ranges. ToF analyzers act as high-pass filters: All energies above a certain cutoff (defined by the potential of the drift tube) can pass the ToF section and reach the detector. In turn, the total time of flight of electrons that travel through the drift section can be larger than the period T of the photon source. For synchrotron radiation sources the period T can be very different, depending on the operation mode. The majority of storage rings provides $T = 2$ ns (corresponding to a temporal filling pattern of 500 MHz), others provide $T = 10$ ns (100 MHz machines, like, e.g., MAX IV), $T = 200$ ns (5 MHz filling, like PETRA-III in 40-bunch mode) or $T = 1$ μ s (1 MHz filling, like BESSY-II in single-bunch mode).

For low drift energies (as needed for high energy resolution) and large widths of the kinetic-energy spectrum, the time of flight τ of the electrons in the ToF analyzer can cover a range larger than 1 μ s. Then, the effect of ‘temporal aliasing’ can occur, *i.e.* electrons with time of flight differing by multiples of T from the probe electrons coincide on the time axis of the ToF spectrum. The time-resolving detector cannot distinguish whether a recorded electron was travelling a time of τ or $\tau+nT$ (with n a natural number). The detector is triggered by the bunch clock of the storage ring, *i.e.* the trigger pulses come in with a period of T . Then, fast electrons released at time t_0 can overtake slower electrons from previous pulses at t_0-T , t_0-2T , t_0-3T etc.

Figure 1 shows two examples. In the first case [Fig. 1(a,b)] the true (wanted) signal [marked (1)] is superimposed by three artefact signals (2-4). These fall into the same time interval (modulo T), but have different energies, visible in the smaller diameters of the k -distribution in Fig. 1(a). In the $k_{||}$ -vs- τ section, Fig. 1(b), signals (1) and (2) show a parabolic-shaped outer rim. Signal (1) with the largest diameter corresponds to time of flight $\tau = t_0$, whereas (2) lies on the low energy side of pattern (1), with $\tau = t_0 + T$. Signals (3) and (4) show a straight rim in Fig. 1(b), indicating that these electrons have much higher kinetic energies, with the time condition $\tau = t_0 - nT$. Indeed, signal (4) shows a series of core levels, visible as horizontal stripes, falling into this time interval. These high-energy signals are caused by admixtures of higher-order radiation in the photon beam. The dominant contribution is the third harmonic ($3 h\nu$). Fig. 1(c) shows a situation, where a core level signal (6) falls into the time window of the valence photoelectrons (5). The small spots close to the rim of the image are the Γ -points of a high-mobility quasi-two-dimensional electron system (with strong spin-orbit coupling) at the interface of a disordered LaAlO_3 film deposited on a KTaO_3 (001) surface (details, see Ref. [17]).

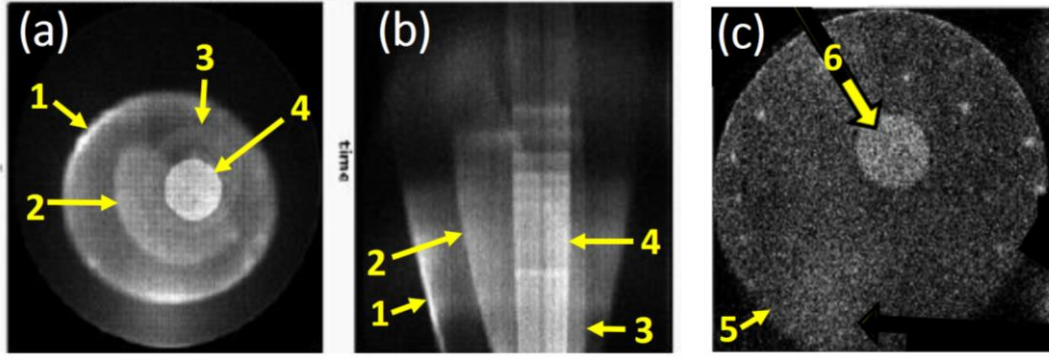


Fig. 1. Momentum patterns overlapping due to the ‘temporal aliasing’ effect; (a,c) $k_x - k_y$ sections and (b) $k_{||}$ -vs- τ representation. The largest pattern (1) corresponds to the electrons of interest with time-of-flight $\tau = t_0$. Pattern (2) represents slower electrons with $\tau = t_0 + T$ [T is the period of the photon pulses]. Patterns (3,4) correspond to faster electrons, which fall into the same time interval due to the time condition $\tau = t_0 - nT$. The intense small disc (4) in (a) corresponds to a series of fast core-level electrons, visible in (b) as horizontal stripes. These fast electrons are released by higher-order admixtures in the photon beam. In (b) patterns (1) and (2) show a parabolic outer contour, whereas (3) and (4) appear straight. The latter electrons are much faster than the true signal and hence they represent a shadow image of the aperture (small circular areas in (a,c) and linear outer contour in (b)). In (c) a core-level signal causes the artefact signal (6), superimposed to the valence-band signal (5).

In conclusion, high-energy applications of the ToF-MM method can suffer from strong artefact signals, when the photon beam contains significant admixtures of higher-order photons. Faster electrons can fall into the same time interval as the true signal when their time of flight obeys $\tau = t_0 - nT$. Likewise, slower electrons can be superimposed with the true signal, when they fulfil the condition $\tau = t_0 + T$. Figure 1 shows how strong these artefacts can show up in the momentum distributions. The purpose of the present development was to implement a compact dispersive bandpass filter, which eliminates such artefact intensities.

II.B The asymmetric dodecapole as versatile electron-optical element

We have chosen the dodecapole as dispersive pre-filter because it is capable of generating a number of multipole fields and enables aberration correction up to 3rd order. The particle-optical properties of 12 electrodes in a dodecagon configuration have been studied in detail by Boerboom et al. [14,15]. The most important features of the electrostatic dodecapole are: deflection in two perpendicular directions by dipolar fields, quadrupole focusing and stigmatization, correction of second- and third-order aberrations, and two-directional focusing. A unique advantage is that several of these applications can be effected simultaneously by superposition of multipole field arrays. First-, second- and third-order focusing can be independently controlled by appropriate settings of the voltages applied to the electrodes. The influence of the fringing field is of fourth-order and thus can be neglected in a third-order approximation.

Figure 2(a) shows a schematic of the asymmetric dodecapole. Depending on the size of the recorded k -range and the pass energy, the beam diameter in the centre of the dodecapole can be very large. Therefore, its geometry has been chosen such that the deflecting field is

homogeneous in a range as large as possible. Otherwise the momentum image located in the centre of the dodecapole would be distorted upon deflection. The equipotential lines in Fig. 2(b) show that the field is homogeneous in a large area of $\sim 80\%$ (marked by the dashed lines) of the total cross section. For comparison, Fig. 2(c) shows the electric field in a conventional octopole unit with the same outer dimensions as in (b), assuming that the centres of the rods lie on the outer contour of the unit. Clearly, the homogeneous region is much smaller, $\sim 50\%$ of the total cross section.

The dodecapole enables the superposition of three multipole fields, the horizontal dipole field (d) and two quadrupole fields (e,f), rotated by 45° with respect to each other. These have the function of a (weak) cylinder lens with selectable azimuthal orientation, compensating for astigmatism. Figs. 2(g,h) show equipotential lines for the superposition of the dipole field (b) with the quadrupole fields (f,e).

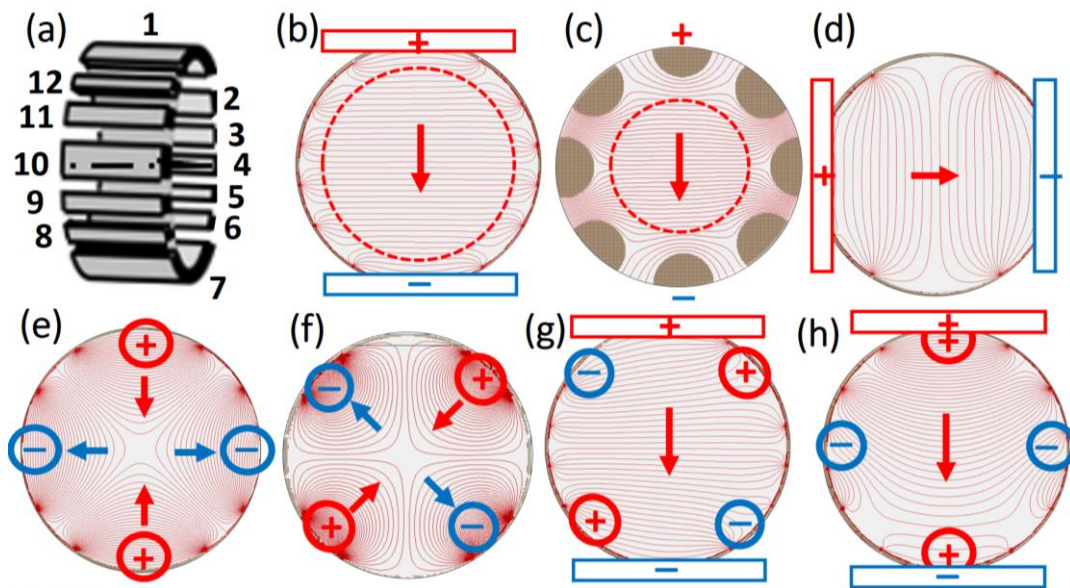


Fig. 2. (a) Schematic view of the asymmetric dodecapole. (b) Calculated potential distribution in the center cross sectional plane of the dodecapole; the dispersive plane is perpendicular. The arrow denotes the deflecting (dipole) field, which causes the energy dispersion. (c) For comparison, dipole field created by a conventional octopole deflector/stigmator with same outer dimension as in (b). (d-h) Correcting multipole fields: (d) Horizontal dipole field correcting for beam position; (e) quadrupole field oriented at $0^\circ/90^\circ$ and (f) quadrupole field oriented at $\pm 45^\circ$ correcting for astigmatism. (g) and (h), examples for the superposition of the deflector field (b) and the quadrupole fields (e) and (f), respectively.

II.C The asymmetric dodecapole as bandpass filter

In the limit of small deflection angles, the homogeneous field (marked by the arrow in Fig. 2(b)) deflects the electrons on parabolic trajectories. First we have performed ray-tracing calculations in order to elucidate the resolving power for different geometries and deflection angles. Figure 3 shows a selection of results for a favourable geometry and a deflection angle of 4° . Lens group 1 focuses a magnified real-space image of the sample (sa) in the 1st Gaussian plane (GP1), where the field aperture (FA) is located. This aperture has two functions: It selects

the diameter of the observed region-of-interest (ROI) on the sample, independent of the size of the illuminating photon beam. Moreover, FA has the function of an entrance aperture of the bandpass filter. The transfer lenses 2 and 3, upstream and downstream of the dodecapole (dod) generate a k -image with parallel rays in the center of the dodecapole and further an image of FA in the plane of the selector aperture SA. SA has the function of the exit aperture of the bandpass filter. SA blocks electrons that are too slow or too fast [trajectories in Figs. 3(a) or 3(c,d)]. Only if the electrons have a kinetic energy close to the pass energy, in this set of simulations 400 eV, they will pass the small aperture SA and are finally imaged onto the delay-line detector DLD by lens 4, Fig. 3(b).

Systematic simulations (using SIMION 8.0 [18]) showed that an impact angle of 2° with respect to the symmetry axis of the dodecapole is a good compromise between sufficient resolution and small aberrations. For such a small angle, the fringe-field effects at the entrance and exit of the dodecapole are negligible. The total deflection angle is then $\alpha = 4^\circ$ and for a distance of 150 mm from the dodecapole to the exit aperture (SA) the beam displacement is 10 mm. Such a small displacement is compatible with a linear vacuum vessel and linear mumetal tube for magnetic shielding of the entire unit. Downstream of SA, a short octupole deflector / stigmator directs the beam by -4° parallel to the original optical axis. Here the beam size is very small so that this second deflection is much less demanding than the deflection in the dodecapole, where a large k -image is located.

Like in every electron spectrometer, the energy resolution depends on the pass energy E_{pass} (= kinetic energy in the dodecapole) and the sizes of entrance and exit apertures, FA and SA. To keep the parameter space small, we restricted the systematic simulations to the symmetric case, where the lateral magnification between FA and SA equals 1. When aiming at maximum energy resolution, it may be advantageous to deviate from this condition. When using the device as bandpass pre-filter in a ToF-MM, we usually set the resolution to 5-10 %. In the given example of $E_{\text{pass}} = 400$ eV the resulting width of the bandpass of 20 – 40 eV is sufficient to eliminate all unwanted energies from the spectrum. The final energy resolution is reached in the ToF section. For this operation mode a diameter of FA and SA in the range of 500 – 1000 μm is sufficient.

By reducing pass energy and slits size, the dodecapole arrangement can also be used as dispersive energy filter without subsequent ToF analysis. The present prototype with 4° deflection angle has been tested experimentally at pass energies and aperture sizes down to ≤ 20 eV and 100 μm , respectively. This combination yields a resolution well below 1 eV. It is crucial for this mode that a large fraction of photoelectrons is focussed into the small circular entrance aperture. This demands on the one hand a high electron-flux density emitted from the sample, *i.e.* a small photon footprint. On the other hand, the spherical aberration of lens group 1 must be minimized, in order to provide a small image of the photon spot in the first Gaussian plane GP1. In the k -imaging mode a maximum possible solid angle interval is aimed at, demanding a large diameter of the k -image in the first reciprocal image plane RP1 (cf. left side of Fig. 3). In Sec. II.D we will elucidate which maximum sizes of solid angles can be accepted by lens 1.

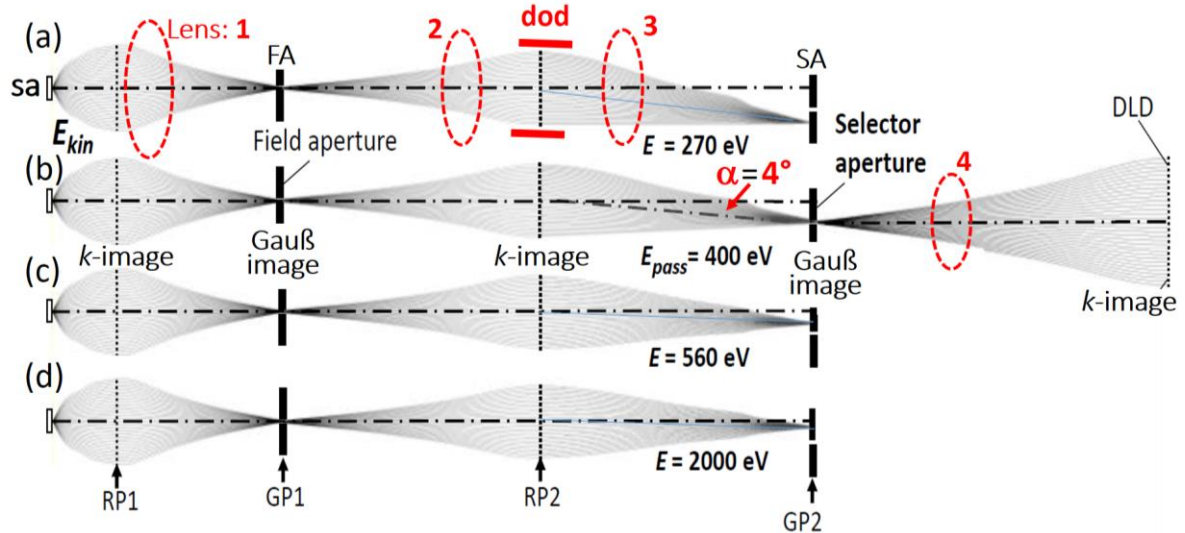


Fig. 3. Ray-tracing simulations of the asymmetric dodecapole for 4 different pass energies as stated in panels (a-d). The dodecapole (dod) is integrated in a realistic lens system of a momentum microscope; lens groups (1-4) schematic. The field aperture (FA) and selector aperture (SA) serve as entrance and exit aperture of the bandpass spectrometer. Lens 1 focuses the first intermediate image of the sample (sa) into the first Gaussian plane (GP1), where FA confines the region-of-interest on the surface. Lens 2 focusses a k -image into the center plane of the dodecapole and lens 3 focuses the second real-space image in Gaussian plane (GP2). The selector aperture (SA) selects electrons in the desired energy interval, here centered at the pass energy $E_{\text{pass}} = 400$ eV (b). Lens 4 focusses the final k -image onto the delay-line detector (DLD). Electrons which are too slow or too fast are deflected too strong (a) or too weak (c,d) and cannot pass the aperture SA. (Ray tracing using SIMION 8.0 [18])

The present study primarily aimed at a simple and compact bandpass pre-filter. Hence, we did not systematically vary the *deflection angle* α in the simulations. Nevertheless, in this first approach, one property of the asymmetric dodecapole became clear. Up to moderate angles, the dispersion increases linearly with α . Hence, the case shown in Fig. 3 but with $\alpha = 20^\circ$ would already yield a resolution of 0.5 % for a slit size of 200 μm . For $E_{\text{pass}} \leq 50$ eV this yields a resolution of ≤ 250 meV, which fits well to the typical bandwidth of hard-X-ray beamlines. The higher energy resolution due to the larger angle comes at the expense of lower k -resolution. However, the large k -field of view (much larger than the solid angles accepted by conventional hemispherical analyzers) is essentially retained, see next Section. In turn, a dodecapole-based imaging momentum microscope (without subsequent ToF analysis) with moderate k -resolution for the X-ray range is possible. Such an instrument would be extremely compact in comparison with hemispherical HARPES spectrometers. Therefore, larger deflection angles may be of interest for future developments in the field of hard-X-ray angular-resolved photoelectron spectroscopy (HARPES).

II.D Solid-angle acceptance of the asymmetric dodecapole

One central criterion for the efficiency of HARPES instrumentation is the accepted solid angle of the electron distribution emitted from the surface. In earlier work [7,16,19], we have considered this point in much detail, in particular comparing the possible solid angles for ToF momentum microscopes and conventional hemisphere-based momentum microscopes and

spectrometers. The general message of these studies is that the ToF instruments are superior in terms of angular acceptance because they do not need small apertures or entrance / exit slits confining the size of the beam and thus clipping part of the signal. Instead, the energy resolution of a ToF instrument is defined by the width of the ‘isochronous plane’ at the entrance of the ToF section. Hence, for such instruments the repetition period, the time resolution and the transmitted energy interval are the crucial parameters that determine the energy resolution. Since the instrument described here can be considered as ‘dispersive-plus-ToF’ hybrid instrument, it is not a priori clear, how the dodecapole instrument compares in this scenario.

In order to elucidate this question and quantify the solid-angle acceptance of the dodecapole setup shown in Fig. 3, we have performed simulations in six different operational regimes: the classical *extractor-MM mode*, the *zero-field mode* with extractor being switched off, and the *repeller-MM mode*, where the front lens is used as retarding lens. The repeller mode and to some extent the zero-field mode facilitate suppressing the space-charge interaction with the slow electrons [20]. All three modes were studied both in the hard- and soft-X-ray regimes.

Figure 4 shows selected results for kinetic energies of $E_{\text{kin}} = 1$ keV (a-c) and 6 keV (d-f), being typical for the two spectral ranges. The figure shows calculated trajectories in the region between sample (sa) and field aperture (FA), which serves as entrance aperture of the dodecapole spectrometer. The criterion was that the diameter of the Gaussian image in the center of FA is not larger than 1 mm (assuming a photon spot size of 50 μm). With diameters of the k -images of 18 and 20 \AA^{-1} , the *extractor mode* (field +3.3 kV/mm) yields the largest solid angle, corresponding to polar angular ranges of $\theta = 0\text{-}35^\circ$ and $0\text{-}15^\circ$, respectively (Figs. 4(a,d)). Note that the equation $k_{\parallel} = 0.512 \sin \theta \sqrt{E_{\text{kin}}}$ relates the solid angle with the maximum observable transversal momentum. The second row shows the *zero-field mode* (0 kV/mm) with sample and extractor are at the same potential. This mode is especially useful for samples with 3D structure like cleaved microcrystals, operando architectures or large off-normal emission angles. Here, the diameters of the k -images are 7.6 and 13.5 \AA^{-1} , corresponding to polar angular ranges of $0\text{-}14^\circ$ and $0\text{-}10^\circ$, respectively [Figs. 4(b,e)]. In the *repeller mode*, bottom row, a specially tailored field is formed in the region between sample and first electrode, such that right in front of the sample a retarding field of -100 and -150 V/mm is generated. In this case, the diameters of the k -images are 11 and 17.4 \AA^{-1} , corresponding to polar angular ranges of $0\text{-}20^\circ$ and $0\text{-}13^\circ$, respectively; Fig. 4(c,f).

Owing to its high collection efficiency, the extractor mode yields the largest angular acceptance. However, the results for the zero-field and – even more – the repeller mode are surprising in the context of the common view of cathode-lens instruments. Let us consider the effect of the extractor field: The extractor-type front lens generates a virtual image of the sample in a distance of roughly twice the gap distance between sample and extractor [21]. At the ‘virtual sample’ position the electrons start with much higher energy and much smaller angular divergence than on the real sample. In the X-ray range the initial kinetic energy is already quite high and the angular interval for a given transversal momentum is smaller than in low-energy PEEM or MM.

This argument may explain the comparatively large observable transversal momentum of the zero mode, but at first sight the high angular acceptance of the repeller mode (for 6 keV the

polar-angular acceptance is 87 % of that for the extractor mode) is puzzling. It is explained by a simple rule of particle optics: Converging lenses can be both, accelerating and retarding. Hence, the repeller mode constitutes a focussing lens, too. The focussing action of the retarding field close to the sample surface is visible in the bottom-left insets of Figs. 4(c,f). In turn, the repeller mode is characterized by a large collecting efficiency, significantly higher than the zero-field mode. The outstanding property of this mode is its strong reduction of the space-charge effect (see, e.g. Figs. 5 and 6 in [20]). This mode will play an important role in femtosecond time-resolved photoemission experiments, especially using X-ray pulses from FEL sources. The retarding field close to the sample rejects all slow electrons and eliminates them from the beam within $<100 \mu\text{m}$ from the sample surface. The fast photoelectrons, in contrast, are even focussed by the short-range repelling field as visible in the two insets at the bottom of Fig. 4.

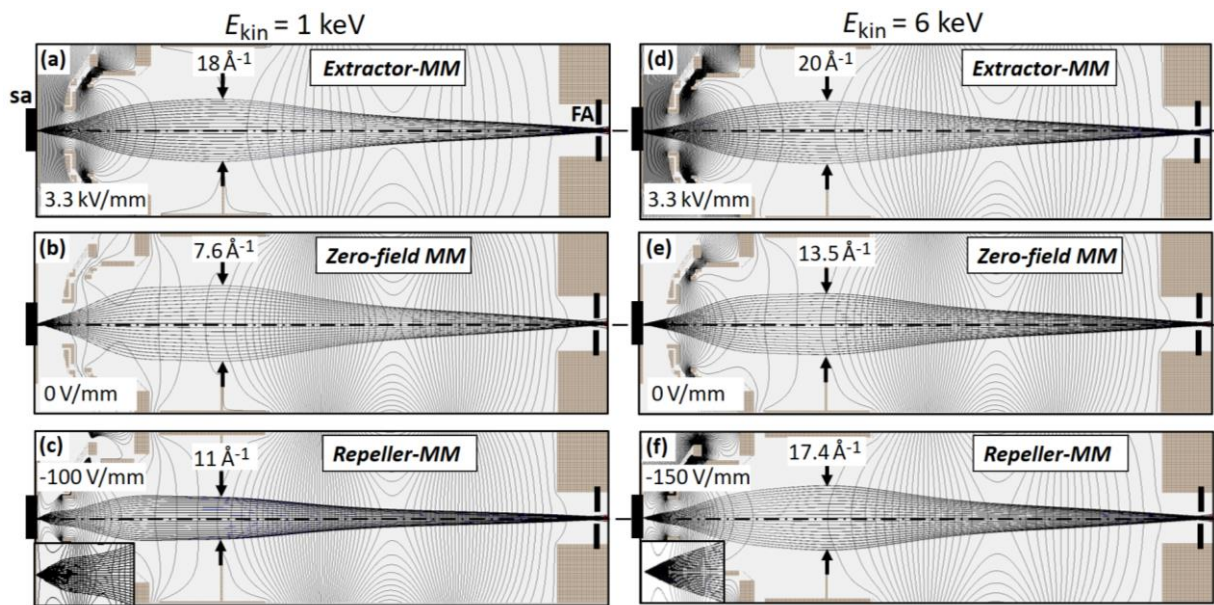


Fig. 4. Ray-tracing simulations of the first lens group between sample surface (sa) and 1st Gaussian image plane, where the field aperture (FA) is located. (a-c) and (d-f) show results at typical soft- and hard-X-ray energies, 1 and 6 keV, respectively. The three rows correspond to the extractor mode with accelerating field of +3.3 kV/mm (a,d), the zero-field mode with 0 V/mm (b,e), and the repeller mode with -100 V/mm (c) and -150 V/mm (f). The accepted k_{\parallel} -ranges are stated in the panels; the criterion is that the Gaussian image in FA has a diameter of $\leq 1 \text{ mm}$ (assuming a photon spot of $50 \mu\text{m}$). (Ray tracing using SIMION 8.0 [18])

The repeller mode offers a special advantage when studying samples with low conductivity. In X-ray photoemission the major contribution to the photocurrent stems from the secondary-electron signal at low energies. A retarding field of the order of 100 V/mm redirects a large fraction of electrons back to the spot where they had been emitted. This significantly reduces electrostatic charging caused by depletion of electrons in the surface region. By appropriate tailoring of the repeller field (with a saddle point slightly below the energy of interest), it would be possible to redirect all electrons except for the wanted probe electrons.

We conclude Sec. II by coming back to the question posed in II.C, concerning the interplay of the accepted solid angle, the deflection angle α and the resolution of the bandpass filter. Like

in every dispersive energy analyzer, the resolution is proportional to E_{pass} and to the sizes of entrance and exit apertures. The sizes of the Gaussian images in Fig. 4 can be reduced by a lower magnification set by lens group 1, which in turn reduces the diameter of the reciprocal image. In other words, the resolution can be increased by sacrificing k -space acceptance. At typical X-ray beamlines the footprint of the photon beam on the sample is of the order of 50 μm or better. Given lateral magnifications in Fig. 4 between 3 and 5, the image of the photon spot is only 150 – 250 μm , when the accepted k -range (and hence the spherical aberration) is sufficiently small.

III. Performance of the dodecapole bandpass filter in a time-of-flight momentum microscope using hard-X-ray synchrotron radiation

III.A Bandpass-filtered momentum microscope with asymmetric dodecapole

Figure 5 shows a schematic view (a) and ray-tracing calculation (b) of the complete prototype momentum microscope including the dodecapole. The instrument comprises 4 zoom lens groups; lens 1 is the unit studied in Fig. 4, lenses 2 and 3 are the transfer lenses in the entrance and exit arms of the dodecapole arrangement (Fig. 3) and lens 4 projects the image onto the delayline detector (DLD). The optics comprises three octupoles serving as deflector/stigmator units, the first and second acting on the k - and Gauss-image and the third (behind the exit aperture SA of the dodecapole unit) for directing the beam parallel to the original optical axis. CA, FA and SA denote three sets of selectable and adjustable apertures, contrast aperture in the back-focal plane (reciprocal plane RP1), field aperture in the first intermediate image (in Gaussian plane GP1) and selector aperture (in plane GP2). The aperture arrays FA and SA comprise auxiliary fine TEM-grids for easy adjustment of the Gaussian planes. In the plane RP1 the k -images have diameters of up to 20 mm, hence the CA grid is a hexagonal array of small holes.

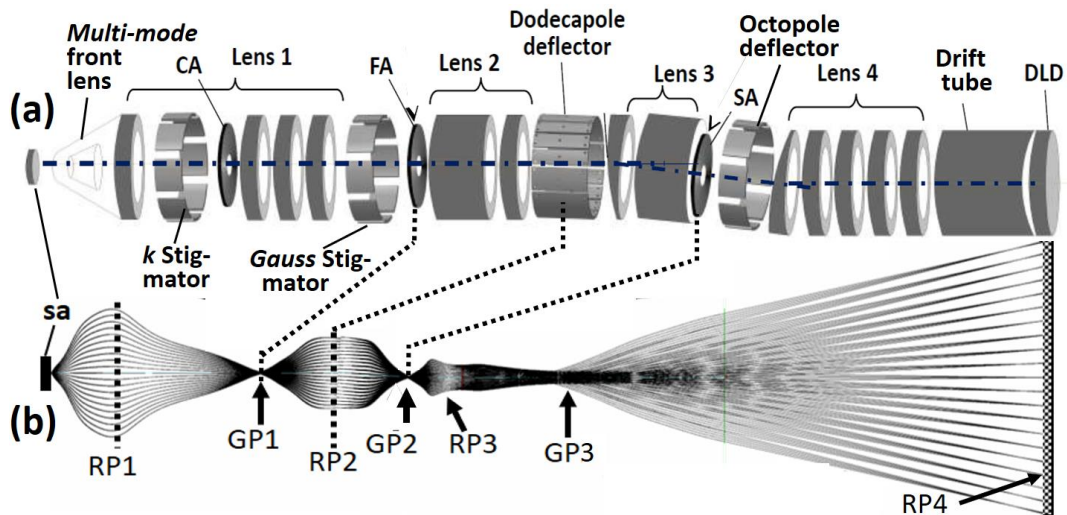


Fig. 5. Bandpass-filtered time-of-flight momentum microscope with dodecapole. (a) Schematic sketch with assignment of the elements; (b) Ray-tracing calculation (using SIMION 8.0 [18]). CA, FA and SA denote contrast aperture, field aperture and selector aperture; the latter two are piezomotor-driven arrays of 16 apertures of different sizes. GP and RP denote the Gaussian and reciprocal image planes. DLD denotes the delayline detector.

In a modified setup we placed an array of contrast apertures for PEEM mode in the conjugate plane RP2, where the size of the k -image is smaller. The instrument can focus real-space or momentum images of the photoelectrons on the delay-line detector (DLD), just by varying lens settings. For real-space imaging of a very large field-of-view up to >5 mm, the front lens is adjusted such that the first reciprocal image RP1 is shifted into the plane of FA. Then, RP and GP are interchanged and a real-space image is focused on the DLD. This is particularly important for ToF X-PEEM, *i.e.* spatial imaging on a core-level signal.

To conclude, the electron-optical system shown in Fig. 5 enables momentum microscopy, (sub-) μm HARPEs using an array of 16 field apertures, full-field photoelectron diffraction and high resolution X-PEEM. The new front lens combines the conventional extractor mode (for maximum k -field of view) with the zero-extractor-field mode (for 3D structured samples) and the repeller mode (for space charge suppression). In all these operational modes the dodecapole bandpass pre-filter enhances the signal-to-background ratio and eliminates higher-order contributions in the photon beam. The instrument works for kinetic energies up to $E_{\text{kin}} \geq 8$ keV.

III.B Performance of the bandpass filter in the hard-X-ray range

The high-energy momentum microscope sketched in Fig. 5 is installed at beamline P22 of PETRA-III (DESY, Hamburg). Figure 6 shows a collection of typical results including spectra and core-level photoelectron diffraction patterns. The spectra demonstrate the effect of the bandpass filter: The signal of interest, here the Mo $2p$ fine-structure doublet (a) and the W $3d_{5/2}$ (c) and P $2p$ core levels (e) are located in the center of the transmitted energy window. The bandpass filter suppresses energies outside of this window. The energy resolution is defined by the time resolution and drift energy in the ToF analyzer.

For strong, isolated core level signals like in Fig. 6(a,c) the transmitted electron distribution is dominated by the core-level signal itself. In these examples the countrate in the DLD was $> 10^6$ counts per second, so that the Mo $2p$ and W $3d_{5/2}$ photoelectron diffraction patterns could be observed in real time with a framerate of a few seconds. Without the bandpass filter, the majority of electrons reaching the DLD does not originate from the core-level of interest. In this case, saturation of the delayline detector limits the recording speed.

Spectral selection by the bandpass filter is also advantageous in cases, where a weak core-level signal of interest is framed by stronger signals from other core levels. Such an example is depicted in Fig. 6(e), showing the P $2p$ signal of 8% phosphorous in a GaAs host lattice. Here the surrounding lines within the bandpass are effectively suppressed in intensity. The same argument applies that the saturation of the DLD is strongly reduced so that the effectively usable intensity of the phosphorous dopant is substantially increased, in comparison with the measurement without the bandpass filter. Figs. 6(a,c) and (e) have been recorded with $E_{\text{pass}} = 400$ eV and 600 eV, respectively.

Yet, the most important effect of the bandpass is the elimination of higher-order artefacts like those in Fig. 1. This is demonstrated by the examples on the right-hand side of Fig. 6. This column shows the X-ray photoelectron diffraction (XPD) patterns corresponding to Mo $2p_{3/2}$ peak (b) and W $3d_{5/2}$ (d,f), both for the (110)-surface. The latter two images show the circular dichroism asymmetry in the core-level diffractogram (for details, see [22,23]). Fig. 6(f) shows

the same pattern as (d), but recorded in the zero-extractor-field mode. Note that image quality and contrast are the same in both dichroism patterns. Only the field-of-view is reduced in the zero-field mode, as was predicted by the ray tracing calculations in Figs. 4(d,e). Structural and spectroscopic analysis of dopants in semiconductors is one of the key applications of full-field XPD using the momentum microscopy technique; see examples of Mn in GaAs [24] and Te in Si [25].

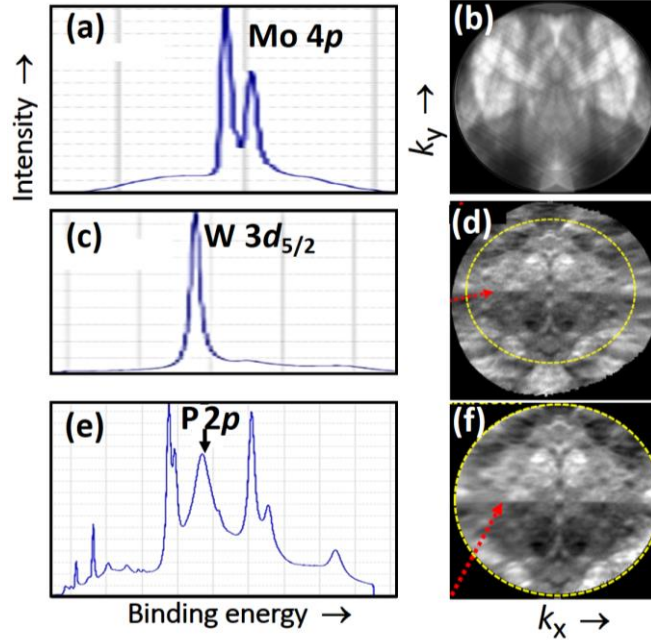


Fig. 6. (a,c,e) Spectral selection by the dodecapole bandpass filter for Mo $4p$, W $3d_{5/2}$ and P $2p$ for GaAsP (with 8% P). (b,d,f) Corresponding X-ray photoelectron diffraction (XPD) patterns with (d,f) showing the circular dichroism signal. (a,b) Recorded for the Mo(110)-surface and (c,d) for the W(110)-surface with $E_{\text{pass}} = 400$ eV; (e) recorded with $E_{\text{pass}} = 600$ eV. Here, the adjacent HAXPES peaks within the bandpass are still strong, but are effectively suppressed in intensity. (f) Same as (d) but recorded in the zero-extractor-field mode, leading to a smaller k -field of view.

The dodecapole arrangement in a momentum microscope as sketched in Fig. 5 can be used as imaging energy filter without subsequent time-of-flight analysis. The pass energy must be reduced and entrance and exit apertures must be sufficiently small. For these measurements we used a helium discharge light source for photoelectron excitation.

IV. Summary and Conclusions

In time-of-flight spectrometers electrons with higher energy than the electrons of interest can pass the spectrometer and reach the detector, similar as in a high-pass filter. If the time of flight of the faster electrons differs by an integer multiple of the period T of the exciting photon pulses, these electrons appear in the same time window as the electrons of interest. This is a well-known phenomenon, usually referred to as ‘temporal aliasing’. In photoelectron momentum microscopy this effect can cause strong artefact signals superimposed to the real signal [16]. Since the time-resolving detector is triggered by the marker of the photon-pulse train, the detector cannot distinguish electrons with time-of-flight differing by $\pm nT$ (n natural

number). The temporal aliasing is especially serious in the X-ray range, because the energy spectrum is very wide (up to several keV) and – in addition – contributions of higher orders of the monochromator and undulator release electrons of even much higher energies. The only way to remove these artefacts is a bandpass filter that cuts off electrons whose energies lie outside of the selected energy band. Without the filter, such undesired electrons contribute to the total signal and can lead to saturation of the detector. In turn, a reduction of the total signal intensity may become necessary, at the expense of the recording efficiency. Hence, besides the elimination of artefacts caused by temporal aliasing, the filter also increases the signal-to-background ratio and recording efficiency. This advantage also holds for other types of spectrometer [26].

Here we described a simple and compact but effective bandpass filter, which eliminates electrons with lower and higher energies. The heart of the device is an asymmetric electrostatic dodecapole, facilitating energy-dispersive beam deflection and correction of image aberrations up to 3rd order. The multipole element is framed by transfer lenses in the entrance and exit branch. Two sets of 16 entrance and exit apertures with different sizes on piezomotor-driven holders enable optimizing transmission and resolution. Gaussian images are located in the entrance and exit apertures, whereas the centre of the dodecapole hosts a k -image. The asymmetric electrode configuration has been designed such that the deflecting dipole field is homogeneous in a large fraction of the cross sectional area. Since the beam deflection angle is as small as 4°, the total beam displacement in the filter is only ~10 mm. The entire instrument is thus very compact and is hosted in a straight mumetal vacuum tube. If integrated into a momentum microscope column, the bandpass filter can be used for imaging in real or reciprocal space.

Ray-tracing simulations elucidated the theoretical performance of the dodecapole filter at typical soft (hard) X-ray energies of 1 keV (6 keV). We studied three operational modes which are used in different types of experiments. The *extractor mode* with a strong accelerating field of +3.3 kV/mm at the sample surface is characterized by maximum k -field diameter of 18 Å⁻¹ (20 Å⁻¹), corresponding to a polar angular range of $\theta = 0-35^\circ$ (0-15°). The *zero-field mode* (0 kV/mm) is advantageous for 2D-structured samples like small microcrystals, operando architectures or large off-normal emission angles. It yields k -images with diameter 7.6 Å⁻¹ (13.5 Å⁻¹), corresponding to a polar angular range of 0-14° (0-10°). In the *repeller mode* specially tailored front-lens electrodes generate a retarding field of -100 to -150 V/mm right in front of the sample. This field eliminates slow electrons from the beam and thus effectively suppresses the dominant part of the space-charge interaction [20]. Despite its retarding action, this mode yields k -images with large diameter 11 Å⁻¹ (17.4 Å⁻¹), corresponding to a polar angular range of 0-20° (0-13°; all values in brackets for 6 keV). Switching between the three modes is facilitated just by different voltage settings of the front electrodes.

The dodecapole bandpass filter is frequently used in a high-energy time-of-flight momentum microscope at the hard-X-ray beamline P22 at PETRA-III (DESY, Hamburg). At pass energies between 400 and 600 eV and entrance and exit apertures with diameters 0.5 to 1 mm this filter transmits a bandpass of 20-60 eV. In this mode as *pre-selector* it effectively eliminates artefacts caused by higher-energy electrons in the ToF analyzer. In a laboratory prototype instrument using a Helium lamp as excitation source, the dodecapole is used as dispersive

energy filter at low pass energies. This mode enables *energy-filtered imaging* without subsequent ToF analysis. When operated at pass energies down to < 10 eV, the filter reached < 500 meV resolution. Owing to phase-space conservation (Helmholtz-Lagrange invariant), this increase of resolution is paid for by a reduction of signal intensity and k -field of view. The overall performance depends on the fraction of photoelectrons accepted by the entrance aperture. The Gaussian image of the photon spot in the entrance aperture is magnified; magnification factors range between 3 and 6. Hence, for high performance the photon spot should be small in order to focus it fully into the entrance aperture of the bandpass filter. These are the same criteria as discussed in context with the hemispherical analyzer used as bandpass pre-filter [7,8].

In the laboratory experiment the performance was limited by the low photon-flux density in the footprint of the unfocussed He lamp on the sample surface. Higher resolution would be possible with higher photon density and/or larger deflection angle of the analyzer. The achieved resolution of 500 meV is sufficient for fast survey studies in the X-ray range.

In conclusion, the present measurements validate the electrostatic dodecapole as a simple but effective bandpass filter. Its dispersion increases linearly with the deflection angle. For the use as pre-filter in a ToF spectrometer, 4° turned out to be a good compromise, providing sufficient resolution, negligible aberrations and a small beam displacement of few mm (being compatible with the standard linear vacuum chamber). Operation as dispersive energy filter without subsequent ToF analysis has been demonstrated but not yet fully explored. The achieved resolution of 500 meV is sufficient for XPS survey studies or Auger spectroscopy. Experiments towards higher resolution are under way.

Acknowledgements

We thank the staff of hard-X-ray beamline P22 (PETRA III, Hamburg), in particular T. Peixoto, A. Gloskovskii and C. Schlueter for excellent cooperation during the beamtimes. Special thanks go to Andreas Oelsner and his team (Surface Concept GmbH, Mainz) for technical support. The ToF-MM development was funded by BMBF (Nos. 05K19UM1 and 05K19UM2) and Deutsche Forschungsgemeinschaft DFG (German Research Foundation) through TRR 173-268565370 Spin +X (projects A02, A05), Project No. Scho341/16-1 and TRR 288-422213477 (project B04).

DATA AVAILABILITY

All data shown within this article is available on reasonable request.

References

- [1] B. P. Tonner, *Energy-filtered imaging with electrostatic optics for photoelectron microscopy*, Nucl. Instrum. Methods Phys. Res., Sect. A **291**, 60–66 (1990).
- [2] B. Krömker, M. Escher, D. Funnemann, D. Hartung, H. Engelhard, and J. Kirschner, *Development of a momentum microscope for time resolved band structure imaging*, Rev. Sci. Instrum. **79**, 053702 (2008).

- [3] M. Escher, N. Weber, M. Merkel, B. Krömker, D. Funnemann, S. Schmidt, F. Reinert, F. Forster, S. Hübner, P. Bernhard, Ch. Ziethen, H. J. Elmers, and G. Schönhense, *NanoESCA: imaging UPS and XPS with high energy resolution*, *J. Electron Spectrosc. Relat. Phenom.* **144–147**, 1179–1182 (2005).
- [4] A. Winkelmann, C. Tusche, A. A. Ünal, M. Ellguth, J. Henk and J. Kirschner, *Analysis of the electronic structure of copper via two-dimensional photoelectron momentum distribution patterns*, *New J. Phys.* **14**, 043009 (2012)
- [5] C. Tusche, A. Krasnyuk, and J. Kirschner, *Spin resolved bandstructure imaging with a high resolution momentum microscope*, *Ultramicrosc.* **159**, 520 (2015).
- [6] C. Tusche, Y.-J. Chen, C. M. Schneider, and J. Kirschner, *Imaging properties of hemispherical electrostatic energy analyzers for high-resolution momentum microscopy*, *Ultramicrosc.* **206**, 112815 (2019).
- [7] G. Schönhense, S. Babenkov, D. Vasilyev, H.-J. Elmers and K. Medjanik, *Single-Hemisphere Photoelectron Momentum Microscope with Time-of-Flight Recording*, *Rev. Sci. Instrum.* **91**, 123110 (2020); doi: 10.1063/5.0024074
- [8] G. Schönhense, K. Medjanik, O. Fedchenko, A. Zymaková, S. Chernov, D. Kutnyakhov, D. Vasilyev, S. Babenkov, H. J. Elmers, P. Baumgärtel, P. Goslawski, G. Öhrwall, T. Grunke, T. Kauerhof, K. von Volkmann, M. Kallmayer, M. Ellguth and A. Oelsner, *Time-of-Flight Photoelectron Momentum Microscopy with 80-500 MHz Photon Sources: Electron-Optical Pulse Picker or Bandpass Pre-Filter*, *J. of Synchr. Radiation* **28**, 1891 (2021); doi: 10.1107/S1600577521010511
- [9] J. Tesch, F. Paschke, M. Fonin, M. Wietstruk, S. Böttcher, R. J. Koch, A. Bostwick, C. Jozwiak, E. Rotenberg, A. Makarova, B. Paulus, E. Voloshina, and Y. Dedkov, *The graphene/n-Ge(110) interface: structure, doping, and electronic properties*, *Nanoscale* **10**, 6088-6098 (2018); doi: 10.1039/c8nr00053k; Specs „KREIOS“: <https://www.specs-group.com/nc/specs/products/detail/kreios-150-mm/>
- [10] F. Matsui, S. Makita, H. Matsuda, T. Yano, E. Nakamura, K. Tanaka, S. Suga and S. Kera, *Photoelectron Momentum Microscope at BL6U of UVSOR-III Synchrotron*, *Jap. J. of Appl. Phys.* JJAP-102449.R1 (2020).
- [11] T. Schmidt, S. Heun, J. Slezak, J. Diaz, K.C. Prince, G. Lilienkamp, E. Bauer, *SPLLEEM: Combining LEEM and spectroscopic imaging*, *Surf. Rev. Lett.* **5**, 1287-1296 (1998); doi: 10.1142/S0218625X98001626
- [12] A. Locatelli, L. Aballe, T.O. Mendes, M. Kiskinova, E. Bauer, *Photoemission electron microscopy with chemical sensitivity: SPELEEM methods and applications*, *Surf. Int. Analysis* **38**, 1554-1557 (2006); doi: 10.1002/sia.2424
- [13] K. Medjanik, O. Fedchenko, S. Chernov, D. Kutnyakhov, M. Ellguth, A. Oelsner, B. Schönhense, T. R. F. Peixoto, P. Lutz, C.-H. Min, F. Reinert, S. Däster, Y. Acremann, J. Viefhaus, W. Wurth, H. J. Elmers and G. Schönhense, *Direct 3D Mapping of the Fermi Surface and Fermi Velocity*, *Nature Materials* **16**, 615 (2017)
- [14] A. J. H. Boerboom, D. B. Stauffer, and F. W. McLafferty, *Theory of the dodecapole*, *Int. J. of Mass Spectr. and Ion Phys.* **63**, 17 (1985); doi 10.1016/0168-1176(85)87037-3
- [15] T. Matsuo, H. Matsuda, H. Nakabushi, Y. Fujita and A. J. H. Boerboom, *Third-order ion optics of an electrostatic multipole lens*, *Int. J. of Mass Spectr. and Ion Phys.* **42**, 217 (1982)
- [16] K. Medjanik, S. V. Babenkov, S. Chernov, D. Vasilyev, B. Schönhense, C. Schlueter, A. Gloskowskii, Yu. Matveyev, W. Drube, H. J. Elmers, and G. Schönhense, *Progress in HAXPES*

performance combining full-field k-imaging with time-of-flight recording, J. Synchr. Radiation **26**, 1996 (2019); doi: 10.1107/S1600577519012773.

[17] M. Zapf, M. Schmitt, J. Gabel, P. Scheiderer, M. Stübinger, G. Sangiovanni, L. Dudy, S. Chernov, S. Babenkov, D. Vasilyev, O. Fedchenko, K. Medjanik, Yu. Matveyev, A. Gloskowski, C. Schlueter, T.-L. Lee, H.-J. Elmers, G. Schönhense, M. Sing and R. Claessen, *Hard X-ray angle-resolved photoemission from a buried high-mobility electron system*, Phys. Rev. B **106**, 125137 (2022); doi: 10.1103/PhysRevB.106.125137.

[18] D. A. Dahl, T. R. McJunkin, and J. R. Scott, *Comparison of ion trajectories in vacuum and viscous environments using SIMION: Insights for instrument design*, Int. J. Mass Spectrom. **266**, 156–165 (2007), <http://www.sisweb.com>, primary author: David J. Manura, SIS (version 8.1/8.0/SL).

[19] C. Kalha, N. K Fernando, P. Bhatt, F. O. L. Johansson, A. Lindblad, H. Rensmo, L. Z. Medina, R. Lindblad, S. Siol, L. P. H. Jeurgens, C. Cancellieri, K. Rosnagel, K. Medjanik, G. Schönhense, M. Simon, A. X. Gray, S. Nemsák, P. Lömker, C. Schlueter and A. Regoutz, *Hard x-ray photoelectron spectroscopy - a snapshot of the state-of-the-art in 2020 (Topical Review)*, J. Phys. Condens. Matter **33**, 233001 (2021) 44pp; doi:10.1088/1361-648X/abeacd.

[20] G. Schönhense, D. Kutnyakhov, F. Pressacco, M. Heber, N. Wind, S. Y. Agustsson, S. Babenkov, D. Vasilyev, O. Fedchenko, S. Chernov, L. Rettig, B. Schönhense, L. Wenthaus, G. Brenner, S. Dziarzhyski, S. Palutke, S. K. Mahatha, N. Schirmel, H. Redlin, B. Manschwetus, I. Hartl, Yu. Matveyev, A. Gloskovskii, C. Schlueter, V. Shokeen, H. Duerr, T. K. Allison, M. Beye, K. Rosnagel, H. J. Elmers and K. Medjanik, *Suppression of the vacuum space-charge effect in fs-photoemission by a retarding electrostatic front lens*, Rev. Sci. Instrum. **92**, 053703 (2021); doi: 10.1063/5.0046567.

[21] L. H. Veneklasen, *The continuing development of low energy electron microscopy for characterizing surfaces*, Rev. Sci. Instrum. **63**, 5513 (1992); doi: 10.1063/1.1143377.

[22] O. Tkach, T. P. Vo, O. Fedchenko, K. Medjanik, Y. Lytvynenko, S. Babenkov, D. Vasilyev, Q.L. Nguyen, T. Peixoto, A. Gloskovskii, C. Schlueter, S. Chernov, M. Hoesch, D. Kutnyakhov, M. Scholz, L. Wenthaus, N. Wind, S. Marotzke, A. Winkelmann, K. Rosnagel, J. Minar, H.-J. Elmers and G. Schönhense, *Circular Dichroism in Hard-X-ray Photoelectron Kikuchi Diffraction observed by ToF Momentum Microscopy*, Ultramicroscopy (2023), in print.

[23] T. P. Vo, O. Tkach, S. Tricot, D. Sébilleau, A. Winkelmann, O. Fedchenko, Y. Lytvynenko, D. Vasilyev, H.-J. Elmers, G. Schönhense and J. Minar, in preparation.

[24] K. Medjanik, O. Fedchenko, O. Yastrubchak, J. Sadowski, M. Sawicki, L. Gluba, D. Vasilyev, S. Babenkov, S. Chernov, A. Winkelmann, H. J. Elmers and G. Schönhense, *Site-specific Atomic Order and Band Structure Tailoring in the Diluted Magnetic Semiconductor (In,Ga,Mn)As*, Phys. Rev. B **103**, 075107 (2021); doi: 10.1103/PhysRevB.103.075107.

[25] M. Hoesch, O. Fedchenko, M. Wang, C. Schlueter, D. Potorochin, K. Medjanik, S. Babenkov, A. S. Ciobanu, A. Winkelmann, H.-J. Elmers, S. Zhou, M. Helm and G. Schönhense, *Active sites of Te-hyperdoped Silicon by Hard X-ray Photoelectron Spectroscopy*, e-print on arXiv:2303.13368, under review.

[26] G. Schönhense and B. Schönhense, German patent DE 10 2020104151 B3 (issued 2021).